PHYSICAL REVIEW B VOLUME 62, NUMBER 15 15 OCTOBER 2000-I

Low-energy-deposited Au clusters investigated by high-resolution electron microscopy and molecular dynamics simulations

B. Pauwels* and G. Van Tendeloo
Elektronenmicroscopie voor Materiaalonderzoek, Universiteit Antwerpen (RUCA), Groenenborgerlaan 171, B-2020 Antwerpen, Belgium

W. Bouwen,[†] L. Theil Kuhn,[‡] and P. Lievens
Laboratorium voor Vaste-Stoffysica en Magnetisme, Katholieke Universiteit Leuven, Celestijnenlaan 200 D, B-3001 Leuven, Belgium

H. Lei and M. Hou
Physique des Solides Irradiés CP234, Université Libre de Bruxelles, Boulevard du Triomphe, B-1050 Bruxelles, Belgium

(Received 4 May 2000)

We investigated the cluster-surface interaction of Au clusters deposited on MgO cubes and on amorphous carbon, and its influence on the morphology of the Au cluster. Au clusters, produced in a laser vaporization source, are deposited with low energy on carbon-coated microscope grids on which MgO cubes are first deposited as substrates. Clusters on the amorphous carbon as well as clusters on the MgO cubes are studied by high-resolution electron microscopy (HREM). The clusters have different morphologies for the two different surfaces, and a dilation of the Au lattice is also measured for the clusters deposited on the crystalline surface of MgO to perfectly accommodate the MgO lattice. Classical molecular dynamics (MD) is applied to model this behavior. Good agreement is found between experimental cross-section HREM images and theoretical images simulated with the multislice technique using the model calculated by MD.

I. INTRODUCTION

A cluster deposited on a surface constitutes a system with specific properties determined by the morphology and the material of the cluster, and the interaction between the cluster and the surface. It is of fundamental importance to study the evolution of the properties with the size of a deposited cluster, e.g., the morphology and, closely related to it, the electron density of states determining its physical and chemical properties. For instance, fivefold symmetry is an example of a morphology uniquely related to clusters. Deposited clusters are also suited as well-controlled building blocks for constructing nanostructures.[1,2] In particular, deposited metal clusters have proven to have potential for a wide range of technological applications, e.g. catalysts,[3] optoelectronics, nanocircuits, magnetic devices, metal-ceramic sensors, mechanically high-strength granular materials, coatings, etc.[4]

Various methods have been applied to study the morphology of single deposited metal clusters on surfaces, e.g., scanning probe techniques [ultrahigh vacuum scanning tunneling microscopy (UHV-STM)[5] and scanning tunneling spectroscopy (STS)[6]], field-ion microscopy (FIM),[7] transmission electron microscopy (TEM),[8] and, in particular, high-resolution electron microscopy (HREM); pioneering work was presented in Refs. 9–11, more recent work includes Refs. 12–19. At present, the atomic resolution achievable with UHV-STM is limited to the facets of the cluster's top layers, and FIM only provides information on the position of the vertex atoms at the cluster facets, whereas HREM makes detailed studies of the cluster morphology possible.

The investigation of the morphology of deposited clusters can be divided into two major groups: clusters nucleated on a substrate by atom deposition, and clusters fabricated in a cluster source and subsequently deposited on a substrate. Clusters fabricated by nucleation on a surface are formed by diffusion and aggregation of adatoms during interaction with the substrate. The preformed clusters differ substantially from those because they have achieved their morphology as ''free'' objects. Inevitably, the preformed clusters interact with the substrate after deposition, and depending on how strong this interaction is, the morphology of the preformed clusters and the substrate can change. Depending on the kinetic energy of the preformed cluster several deposition regimes exist: soft-landing ($E_{\mathrm{kin}}<0.1$ eV/atom), low-energy cluster beam deposition (LECBD) ($E_{\mathrm{kin}}<1.0$ eV/atom), and energetic cluster impact (ECI) ($E_{\mathrm{kin}}>10$ eV/atom).[20,21] In both the soft-landing and LECBD regimes the impact energy is low enough to prevent deformation of the substrate, and the single cluster keeps its identity, whereas in the ECI regime the substrate is damaged and the cluster is completely deformed, losing its identity. Soft-landing and LECBD regimes can be used for growing nanostructured materials[1,2] and ECI is suited for fabricating thin films.[20] In this paper, we shall be discussing the morphology of preformed metal clusters deposited by LECBD.

The structural properties of deposited metal clusters were intensively studied by theoreticians, among the most powerful tools are molecular dynamics (MD) simulations. For a short review see, for instance, Ref. 22. From a fundamental point of view quantum-mechanical MD is the most correct, but it can only be performed for a limited cluster size. For clusters consisting of elements with many electrons the upper limit is approximately 50 atoms. For simulating larger clusters containing many electrons classical MD has to be applied.

In Ref. 23 the authors used quantum-mechanical MD to simulate the ''magic'' Na_8 cluster when it was either deposited on an insulating NaCl(001) surface or on a metallic

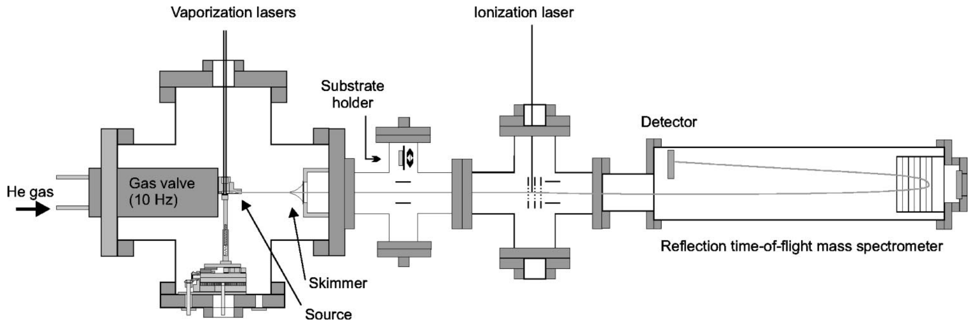

FIG. 1. An overview of the laser vaporization cluster source, mass analyzer, and cluster deposition setup.

Na(110) surface, or brought into contact with another Na_8 cluster in vacuum. They observed that the Na_8 cluster on the NaCl(001) surface remained very stable, and almost did not change its geometric and electronic structure, but on the Na(110) surface it immediately collapsed and formed an epitaxial layer. The interaction between two Na_8 clusters caused them to lose their identity, and form a Na_{16} cluster with a completely different geometric and electronic structure. These MD simulations show how determining the cluster-surface interaction is for the morphology of the deposited cluster, even when the preformed cluster is physically and chemically very stable.

Recently, classical MD simulations of a fcc Cu_{440} cluster deposited at room temperature by LECBD on a fcc Au(111) surface was presented.[24] The evolution of the cluster and surface morphology after the impact was simulated, showing that the substrate is compressed for a short time but maintains its fcc structure, whereas the cluster exhibits strong relaxation effects depending on the impact energy. For the lowest impact energy ($E_{\mathrm{kin}}<0.25$ eV/atom) the cluster adjusts epitaxially to the substrate, and evolves facets. These facets become modified with increasing impact energy, but the epitaxy is maintained until $E_{\mathrm{kin}}=1$ eV/atom. For impact energies $E_{\mathrm{kin}}>1$ eV/atom the Cu cluster wets the Au surface, the cluster morphology is disordered, and there is a 10% mixing of the Au and Cu atoms. The epitaxy causes internal stress in the Cu cluster which is mostly accommodated by the first interfacial layer. Since the interfacial relaxation is closely related to the balance between the cohesive energies, these simulated morphologies are specific for the system of a Cu_{440} cluster on a Au(111) surface, but they illustrate the strong influence of the impact energy even in the narrow range 0.25–1 eV/atom of LECBD on the resulting cluster morphology.

Here we present a combination of HREM studies of the morphology of well-characterized preformed Au clusters simultaneously deposited by LECBD on two fundamentally different types of substrates—amorphous carbon and single crystalline MgO—and classical MD simulations of the observed systems. Substrates of single-crystalline MgO cubes on amorphous carbon were chosen to be able to simultaneously study the differences in morphology of clusters subject to strong and weak interactions with the substrate. MgO is characterized and described in the literature,[25] and it serves as an internal microscope reference for measuring absolute lattice parameters of the clusters. Au clusters consisting of a few up to several thousand atoms are produced by a laser vaporization cluster source.[26] Depositing clusters of the noble metal Au prevented contamination. Furthermore, Au clusters are very well characterized both experimentally and theoretically providing the necessary information for the HREM image analysis and the MD simulations. First, the HREM images were analyzed by standard image analysis simulations, showing that these were insufficient in describing the morphology of all of the cluster layers. Second, the cluster morphology obtained from the HREM image analysis was used as the initial configuration for the MD simulations. Third, the resulting configuration of the MD simulation was used for the HREM image analysis, and a perfect match between the experimentally observed and the simulated morphologies was obtained. By combining these complementary techniques we have been able to study the evolution of the lattice parameters of Au clusters on MgO throughout the cluster layers from the interface to the top showing relaxation, contraction, and dilation.

The paper is structured as follows: In Sec. II the experimental techniques are described; in Sec. II A the sample preparation is presented, and in Sec. II B the HREM technique including image analysis is explained. Section III contains an overview of the MD simulations, Sec. IV a discussion of the results, and Sec. V conclusions.

II. EXPERIMENTS

A. Cluster deposition

The Au clusters are fabricated in a laser vaporization cluster source. Figure 1 shows an overview of the apparatus; it was described in detail in Ref. 26. A pulsed laser ablates material from a target. The supersaturated metal vapor thus formed is cooled by a He gas pulse and expansion which causes condensation of the vapor into clusters. A beam of clusters is setup by several stages of differential pumping. The free-flying clusters are analyzed by time-of-flight mass spectrometry, Fig. 2 shows the size distribution. The pressures in the cluster source and in the time-of-flight mass spectrometer chamber are 10^{-7} and 10^{-9} hPa, respectively. During cluster production these pressures rise to typically 10^{-4} and 10^{-7} hPa, respectively, due to the He gas.

Characteristic for this type of cluster source is that the metal vapor is quenched producing a cold beam of clusters with a temperature lower than 300 K, and the kinetic energy of a cluster is about 0.5 eV/atom. Thus the clusters can be used for low-energy cluster beam deposition.[1,20,27] The clusters are not formed in equilibrium, and they therefore do not

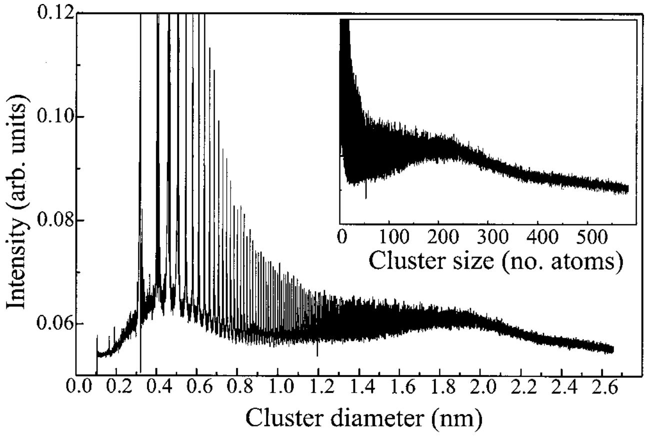

FIG. 2. Size distribution of ionic free Au clusters as observed by time-of-flight mass spectrometry, without correction for the decrease of the detector efficiency for the heaviest clusters. This size distribution thus can have an upper cutoff. The diameter was calculated assuming the clusters to be spherical.

exhibit magic numbers in the mass spectrum. However, by transferring energy to the clusters by photon absorption (delivered by the laser ''ionization laser'' in Fig. 1) they can achieve equilibrium shapes, and the stability as function of number of atoms per cluster can be studied.[28] In the experiments presented here the Au clusters are deposited as prepared directly from the frozen metal vapor.

Figure 2 shows the size distribution of the cationic free Au clusters as measured by reflection time-of-flight (RTOF) mass spectrometry. The RTOF technique measures the abundance as function of number of atoms in the clusters. Assuming the clusters to be spherical and using the Wigner-Seitz radius for Au (1.59 Å),[29] this has been converted to abundance as function of diameter. A large number of small clusters is present in the beam, but the major part of material is concentrated in the larger clusters having an average diameter of approximately 1.9 nm. However, due to decreasing efficiency of the detector for the heaviest clusters, this size distribution has an upper cutoff, such that clusters larger than observed with the mass spectrometer may be present in the beam.

For the sample preparation MgO cubes on amorphous carbon film are used as substrates for the Au clusters. Mg grains are heated in air with a Bunsen burner. When they start to burn, a white smoke is produced. The smoke contains MgO single crystals which are collected on a carbon-coated Cu grid by holding the grid in the smoke. The crystals have always the shape of a cube, and their size is dependent on the temperature at which the grains are heated. The number of cubes is dependent on the time the grid is held in the smoke. In the experiments described here, mostly cubes with sizes of the order of 300 nm are used because they can easily be oriented along a zone axis. The MgO single crystals have the same structure as rock salt (NaCl), and, because of their size, they can be considered bulk materials with a known lattice parameter of 4.20 Å .[25]

A substrate of amorphous carbon with MgO cubes is placed in the cluster beam in the second chamber (see Fig. 1), and Au clusters of all produced charge states are deposited on the surface by LECBD, minimizing the interaction between the clusters and the substrate during impact. The substrate is constantly kept at room temperature, and the clusters are deposited at very low density so they are isolated from each other at the substrate. After deposition the sample is transferred to the transmission electron microscope. Both the Au clusters deposited on the MgO cubes and on the amorphous carbon are studied by HREM.

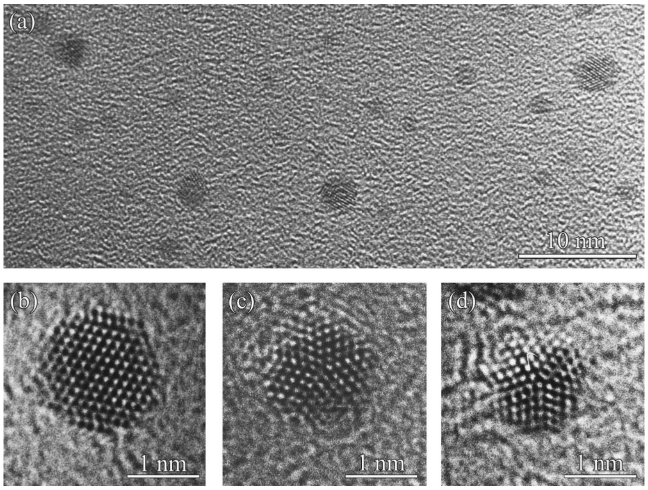

FIG. 3. (a) Overview of clusters deposited on amorphous carbon. The deposition time for this sample was 1.5 min. (b)–(d) Some examples of HREM images of Au clusters deposited on amorphous carbon: (b) shows a cubo octahedron viewed in a [011] direction; (c) and (d) show two images of decahedral particles which consist of five tetrahedra along a [011] zone axis.

B. High-resolution electron microscopy

HREM images are taken with a JEOL 4000 EX microscope, which has a point resolution of 1.7 Å. Other parameters of the microscope which are needed to perform the simulations of HREM images are the spherical aberration constant $C_s = 1.0$ mm, the defocal spread $\Delta f = 8.0$ nm, and a semiconvergence angle $\alpha = 0.55$ mrad. Because of the epitaxial relation between the Au clusters and the MgO, it is possible to orient the MgO cubes along a zone axis at low magnification, and then both the lattices of the clusters and the MgO substrate can be imaged together. For clusters deposited on amorphous carbon, the orientation of the clusters is random, and one has to search for a cluster which has a zone axis along the incident electron beam. The high resolution observations are carried out at a low electron-beam irradiation density (17 pA/cm^2) in order to avoid structural reorientations caused by the electron beam. Most of the time the clusters are stable under the beam; only a few times structural reorientations are observed before the cluster stabilizes.

To obtain a size distribution for the Au clusters on amorphous carbon, image analysis is done using the Kontron KS 400 Version 1.2 image processing software. Because of the amorphous background, which shows many features, it is difficult to separate the clusters from the background and a great deal of image processing is needed. The following steps are performed. An image, as shown in Fig. 3(a), is scanned with a resolution of 300 dpi and 256 (eight-bit) gray levels. Taking into account the enlargement of the microscope, this means that 1 pixel is 0.87 Å. First a shading correction is applied. The original image is smoothed with a low pass filter of size 49 (7×7 pixels, repeated 20 times) to produce a reference for the actual shading correction. When applying this correction a more or less evenly illuminated image is obtained. Then the image is further enhanced by applying a low pass filter of size 9 (3×3 pixels), followed by a contrast enhancement. To perform the image segmentation, a binary image is created using an arbitrary threshold at gray level 100. Hereby image objects with an area less then 30 pixels (or an equivalent diameter of 5.4 Å) are removed because it is not possible to distinguish clusters from features in the amorphous carbon for these sizes. This binary image is used as a mask to measure the objects in the original image. The area, the equivalent diameter, and the coordinates of the center of gravity for each object are produced in pixels. The enlargement of the microscope is known, and the data can be recalculated in nm. All this image processing is done automated, but it is always necessary to verify the results by eye, because sometimes features in the amorphous carbon can be recognized by the program as a cluster. It also happens that the software does not find a small cluster which is visually there.

To evaluate lattice distances in the clusters, the DALI program (Digital Analysis of Lattice Images) is used.[30] The general procedure to measure the distances is as follows: before measuring, a Wiener filter is applied on the experimental images to reduce the noise level. First the positions of maximum intensity are searched. Afterward, to yield a more accurate estimate of the peak positions, a parabolic function is fitted in a region close to the estimated maximum intensities. Fitting with a parabolic function can be done because the intensity profile of a spot is nearly sinusoidal.

The MgO cubes on which the Au clusters are deposited can be considered as bulk material with a known lattice parameter (4.20 Å). The lattice distances in the Au clusters are measured relative to the lattice distances of MgO, and it is possible to study small local variations of the lattice in the clusters. This cannot be done for clusters deposited on the amorphous carbon of the microscope grid, because the exact enlargement of the microscope is dependent on the objective lens current and other microscope parameters, and differs slightly from image to image.

All simulations of HREM images are done with the EMS program,[31] running on a DEC Alpha XP 1000 Workstation. The Au cluster and the substrate are placed in a square supercell of 6 nm in x and y directions perpendicular to the zone axis, which is taken as the z direction. The supercell is taken large enough to avoid influences of the supercell borders on the image. To obtain the right contrast of the substrate, some extra MgO layers are added. First the electron wave function of the model is calculated with a multislice dynamic calculation.[32] The sampling in the x and y directions is always 1024 pixels in each direction, which gives a precision of 5.86×10^{-2} Å between two neighboring points. The thickness of the slices in the z direction is 1.5 or 1.0 Å. Afterward the influence of the microscope on the image formation process is added. Using the electron wave function and the microscope parameters of the JEOL 4000 EX microscope, the HREM images are simulated.[32]

In this contribution a selection of the HREM images is presented. Many more images, both from clusters on amorphous carbon and from clusters deposited on the MgO cubes, were obtained. Figure 3 shows some images of clusters deposited on amorphous carbon. An overview is shown in Fig. 3(a); most of the clusters are not oriented. Only some of them have a simple zone axis along the incident electron beam. Figure 3(b) shows a cubo octahedron along the [011] direction. Decahedral clusters viewed along the [011] zone axis are shown in Figs. 3(c) and 3(d). The fivefold symmetry is clearly seen. Also icosahedral clusters and twinned structures are often observed in Au clusters deposited on amorphous carbon.

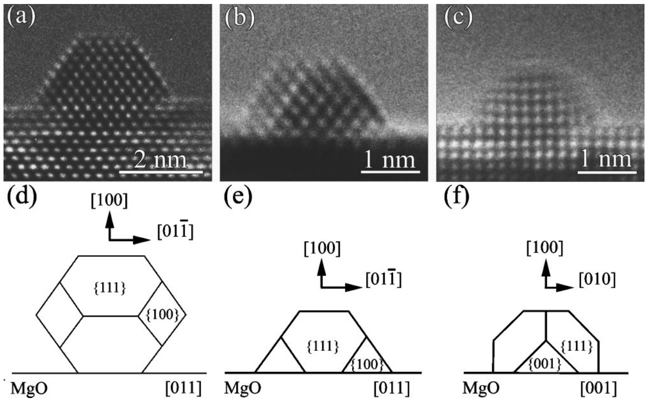

FIG. 4. Au clusters deposited on MgO: (a) HREM image of a truncated octahedral cluster in a ⟨011⟩ zone axis orientation. (b) Half octahedral cluster in a ⟨011⟩ orientation. (c) Half octahedral cluster in a ⟨001⟩ orientation. (d)–(f) Profiles of the clusters shown in (a)–(c), respectively, with an indexation of the crystallographic directions and the faces.

To study the morphology and small lattice dilations of clusters deposited on MgO, projection of the clusters perpendicular to the Au/MgO interface (cross-section) is necessary. Two different orientations are imaged in cross-section view: ⟨011⟩ and ⟨001⟩. Figure 4(a) shows a Au cluster of 2.2 nm in height (distance from the interface to the top of the cluster) and 3.0 nm in width deposited on a MgO cube oriented along the [011] zone axis. Other cross-section images of clusters are shown in Figs. 4(b) and 4(c): (b) shows a cluster in the [011] orientation, while the cluster shown in (c) is a cluster with the same morphology but in the [001] orientation. The corresponding profiles of the clusters with an indexation of the crystallographic directions and faces are shown in Figs. 4(d), 4(e), and 4(f), respectively. The morphology of the cluster shown in Fig. 4(a) is different than the morphology of the other two clusters of Fig. 4. Figure 4(a) is a truncated octahedral cluster, while Figs. 4(b) and 4(c) are truncated half octahedral clusters. This will be discussed in more detail in Sec. IV. In the ⟨011⟩ orientation HREM images are also made of clusters in a top view, parallel to the interface (see Fig. 5).

III. MOLECULAR-DYNAMICS MODEL

In order to understand the internal relaxation induced by the substrate, the atomic configuration in a Au cluster as observed by HREM after deposition is modeled by means of classical MD. Therefore, an accurate knowledge of the atomic positions at the substrate surface is necessary, which is only available in the case of MgO. This is the reason why

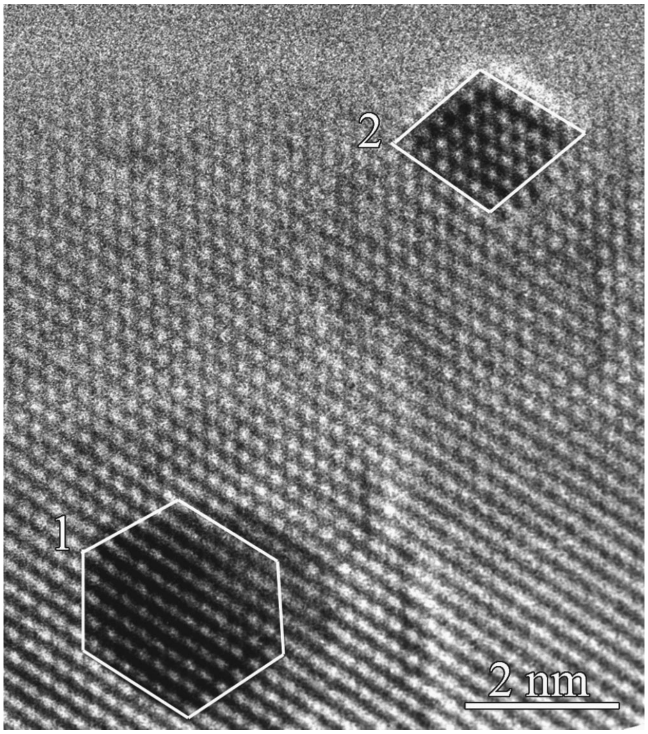

FIG. 5. Image of a MgO cube along the ⟨011⟩ zone axis. Two profiles of octahedral clusters on the surface are visible. Profile 1, which is often seen in plan view images, is from a truncated octahedral particle; profile 2 could be from an ideal octahedron. However such a perfect octahedral cluster is never seen in a cross-section HREM image. Also in top view images, it is observed only a few times.

the present modeling is restricted to the case of a Au cluster, as deposited on MgO and observed at room temperature.

Several ingredients are necessary to achieve a MD modeling. One first needs initial conditions. These are provided by HREM, from which clear information is deduced about the cluster morphology (see Sec. IV) and also about the atomic row positions projected onto the [100] and [110] directions parallel to the interface. Figure 6 shows such a model where the Au cluster morphology is identical to that of the selected cluster [Fig. 4(a)]. Despite the equilibrium lattice mismatch, HREM shows evidence for accommodation at the interface, with most of the distortion absorbed by the cluster. Therefore, in our initial conditions, the interfacial Au atoms are displaced to match exactly the MgO geometrical lattice, and the nearest-neighbor distance in the Au interfacial layer is 2.97 Å.

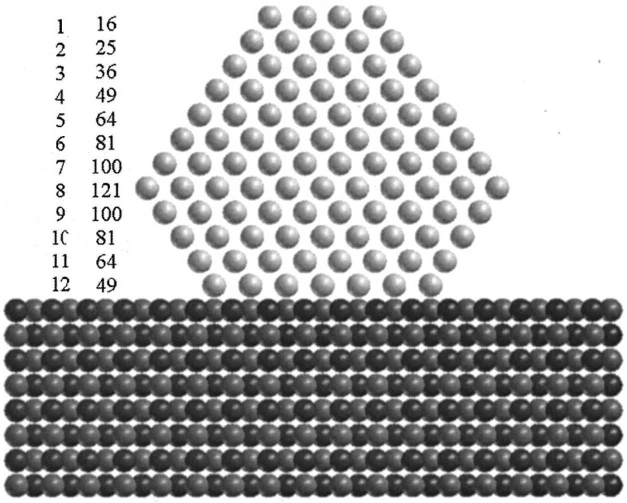

FIG. 6. Initial configuration of Au_{786}/MgO(100). The layer number is given in the first column, and the number of atoms in each layer l in the second column.

One then needs a cohesion model for Au. Those suggested in the literature are numerous, though most generally based either on the embedded-atom model[33] or on the second-moment approximation of the tight binding model.[34] We selected the latter, according to which the configuration energy of the Au system, projected on an atom i, is written as

$$E_i=\frac{1}{2}\sum_{j\neq i} V(r_{ij})-\left[\sum_{j\neq i}\Phi(r_{ij})\right]^{1/2}, \tag{1}$$

so that the total energy of the system is

$$E_T=\sum_i E_i. \tag{2}$$

The summations in Eq. (1) represent the contributions of all other atoms in the system. r_{ij} is the distance between the atoms i and j, and $V(r_{ij})$ is a repulsive pair potential between these atoms. $\Phi(r_{ij})$ describes the sum of squares of hopping integrals between atomic sites i and j. The potential functions are constructed as a series of cubic splines, and their range is limited just beyond the third neighbor distance.[35]

The third ingredient is a tool, which allows one to show the influence of the MgO substrate on the atomic relaxation in the cluster, as can be identified by HREM. We are unaware of reasonable models for the interaction between gold, magnesium, and oxygen at the Au/MgO interface. Therefore, and in view of characterizing the effect of interfacial forces on the internal cluster relaxation, the interaction between interfacial Au atoms and the MgO substrate is modeled by a simple effective harmonic potential. A harmonic force is thus added to each interfacial Au atom, that can be written as

$$\mathbf{F}_{h,i}=k(\mathbf{r}_i-\mathbf{r}_{0,i}), \tag{3}$$

where k is a force constant to be adjusted. $\mathbf{r}_i$ and $\mathbf{r}_{0,i}$ are the instantaneous and epitaxial position vectors of atom i, respectively. One problem is to select a realistic force constant k. In order to find a reasonable range of k values, we first determined the effective atomic force constant of bulk crystalline Au. It is deduced in the harmonic approximation from the experimental value of the bulk modulus as $k_{bulk}=3.84\times 10^2\ \mathrm{J/m^2}$. At the Au/MgO interface, k is taken as a parameter which magnitude is lower than k_{bulk}. Values between $k=0$ and $k=2.0\times 10^2\ \mathrm{J/m^2}$ are considered. The case $k=0$ corresponds to a free cluster with the same morphology (see Fig. 6). A comparison with $k>0$ will help us to understand the influence of the substrate on the internal strain in the cluster.

In the present simulation, the equation of motion of an atom i can be written as

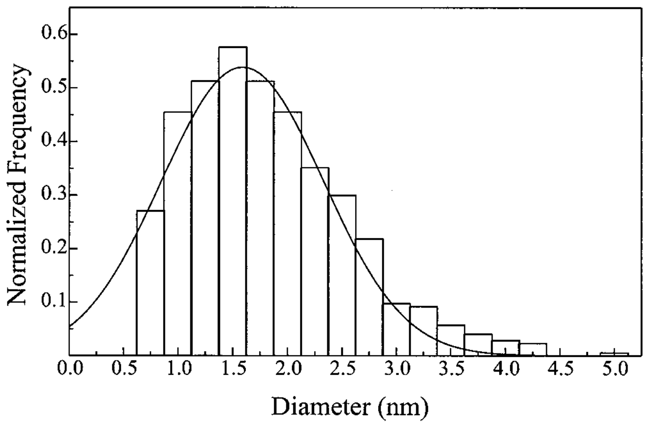

FIG. 7. Size distribution of 694 Au clusters obtained from a sample with a deposition time of 1.5 min. The Gaussian function fitted to the data is also shown.

$$m_i \frac{d^2\mathbf{r}_i}{dt^2} = \mathbf{F}_i - \mu_i \mathbf{v}_i , \tag{4}$$

where $\mathbf{F}_i$ is the force on atom i, which embodies the gradient of the potential [Eq. (1)], and, for interfacial Au atoms, the force contribution given in Eq. (3). The coefficient of the velocity $\mathbf{v}_i$ of particle i is taken as

$$\mu_i = m_i \alpha \frac{(T_i - T_e)}{(T_i + \epsilon)} . \tag{5}$$

α is the inverse coupling time to the thermal bath at temperature T_e, and it is taken to be equal to 1 ps for convenience. T_i is the instantaneous temperature of atom i and m_i is its mass. ϵ is a small constant introduced in order to avoid divergence when the instantaneous velocity tends to zero. It should be noted that the velocity-dependent term in Eq. (4) represents the contribution of an external force on the system. Consequently, the total angular momentum of the cluster may not be preserved.

When the force constant in Eq. (3) is zero, the cluster is free, and cluster rotation is possible. Therefore, in this case, the Newton equations of motion are used rather than Eq. (4) to avoid angular momentum resulting from external forces. Thermalization is then achieved by means of a velocity rescaling procedure.

Starting with the initial configuration shown in Fig. 6, the thermal evolution of the Au cluster is followed during 200 ps. The integration time step is 2 fs, and the temperature of the thermal bath is $T_e = 300$ K. The equilibrium is achieved when there are nothing but statistical temporal variations in the mean kinetic and configuration energies of the system. In practice, it takes about 10 ps to reach thermal equilibrium. Starting somewhat later, the instantaneous nearest-neighbor distances are recorded and accumulated to evaluate their mean values. The mean atomic positions are evaluated as well. In addition, HREM images from the model configuration can be simulated and compared to the real images, as will be discussed below.

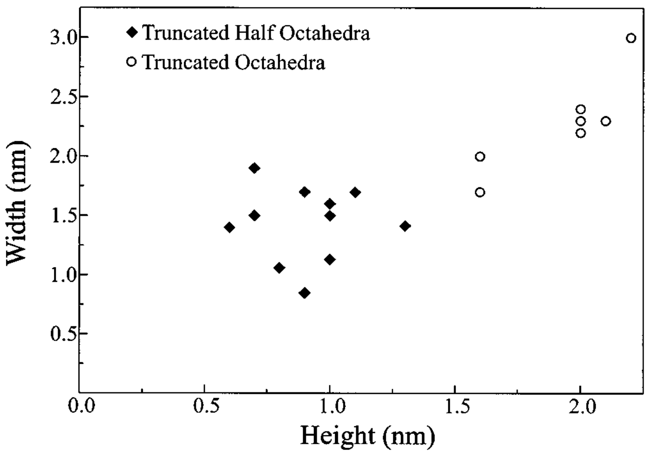

FIG. 8. Graph which shows the cluster morphology in function of the width (distance in ⟨011⟩ view) and the height (distance interface-top) of the clusters.

IV. DISCUSSION

The relations between the cluster structure, morphology, and size distribution in the beam and on the substrate are not obvious. Since the clusters are produced out of equilibrium, no intensity enhancement relates to magic numbers and thus to particularly frequent morphologies. Classical MD predicts metallic clusters of the order of 100 atoms and more to have binding energies only little dependent on their morphology.[36] Quantum-mechanical tight binding models[37] provide similar estimates. This suggests the possible coexistence of several isomers which morphology, once deposited, may be significantly influenced by the substrate. Temperature, in certain conditions, may activate overall rearrangements.[38] On graphite surfaces, every bonding state is occupied, so that a landing metallic cluster only interacts with it via van der Waals forces after impact. These are weak enough that clusters diffuse as a whole at room temperature,[1] and aggregate. In contrast, the interaction with a silica surface is estimated to be much more significant.[39]

Significant cluster-surface interactions may also be expected for amorphous carbon surfaces characterized by states available for bonds. These bonds are directional, but not correlated between neighbors and might influence the cluster structure. Whatever the nature of the interaction is, the interaction energy is sufficient to prevent cluster diffusion, and to allow characterization by atomic scale observation techniques. Hence, even when the substrate surface is structureless (i.e., amorphous), an influence on the cluster structure and morphology cannot be excluded. Significant questions remain. In what follows, however, the Au cluster state after deposition on amorphous carbon and on crystalline MgO will be characterized. These substrates differ from each other by their surface state since MgO microcrystals are pronouncedly ionic, and they display well-defined (100) surfaces.

A. Cluster size distributions on amorphous carbon and MgO

Figure 7 shows the size distribution of 694 Au clusters on an amorphous carbon surface. This size distribution is obtained by TEM from a sample, such as shown in Fig. 3(a), with a deposition of Au clusters for 1.5 min. A Gaussian

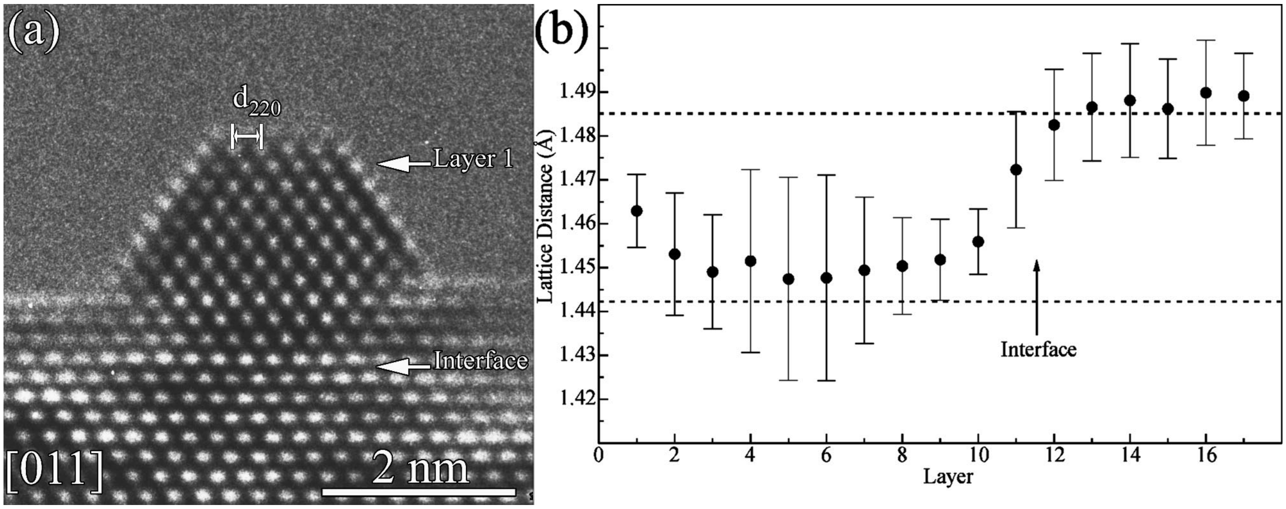

FIG. 9. (a) HREM image of a deposited cluster along the ⟨011⟩ zone axis. The same cluster is also shown in Fig. 4(a). (b) Graph showing the averaged d_{220} lattice spacing in the different layers through the cluster and the substrate. The dashed lines represent the bulk MgO value (1.485 Å) and Au d_{220} value (1.442 Å), and are shown for comparison. Layer 1 is the top layer of the cluster, and the Au/MgO interface is between layers 11 and 12. Looking at the image in (a), one could conclude that the interface Au/MgO is around layer 9, because there is already some contrast of the substrate. This is due to a step in the MgO behind the cluster which is not in focus.

function is fitted to these data. The average cluster size (μ) and the geometrical standard deviation (σ) are determined as 1.59 and 0.74 nm, respectively. The average cluster size and standard deviation for a log-normal fit are 1.71 and 0.77 nm, respectively, and χ^2, which is a measure of the ''goodness of fit,'' was only slightly smaller. Also a size distribution of 514 Au clusters obtained from a sample of which the deposition time was doubled, is fitted by a Gaussian and a log-normal distribution. In this case, a Gaussian function with a mean cluster diameter of 1.90 nm and a standard deviation of 0.82 nm, gave a better fit than a log-normal function with a mean diameter of 2.03 nm and a standard deviation of 0.86 nm. The mean diameters obtained from these TEM samples are in good agreement with the diameter of the larger clusters in the free cluster beam measured in the reflection time-of-flight mass spectrometer. The conclusion is that after the clusters are deposited, they do not significantly coalesce into larger clusters.

A classification is made of all cross-section HREM images of Au clusters deposited on MgO in the two different morphologies (see Fig. 8). It is clearly seen that the larger clusters with an average height of 1.92±0.24 nm and an average width of 2.27±0.40 nm are truncated octahedra, while the smaller clusters (average height 0.94±0.22 nm and average width 1.42±0.30 nm) are truncated half-octahedra.

Comparing the graph of Fig. 8 with the size distribution of Fig. 7, it is seen that the average height and width of the clusters deposited on MgO are of the same size as the average cluster sizes found for the clusters on amorphous carbon. The interaction between a Au cluster and the MgO surface is larger than the interaction of a Au cluster with the amorphous carbon. For clusters deposited on amorphous carbon there is no coalescence, so it can be expected that the coalescence between clusters deposited on the MgO cubes is also limited. This is also supported by the fact that clusters larger than 3 nm are not observed. If there is coalescence

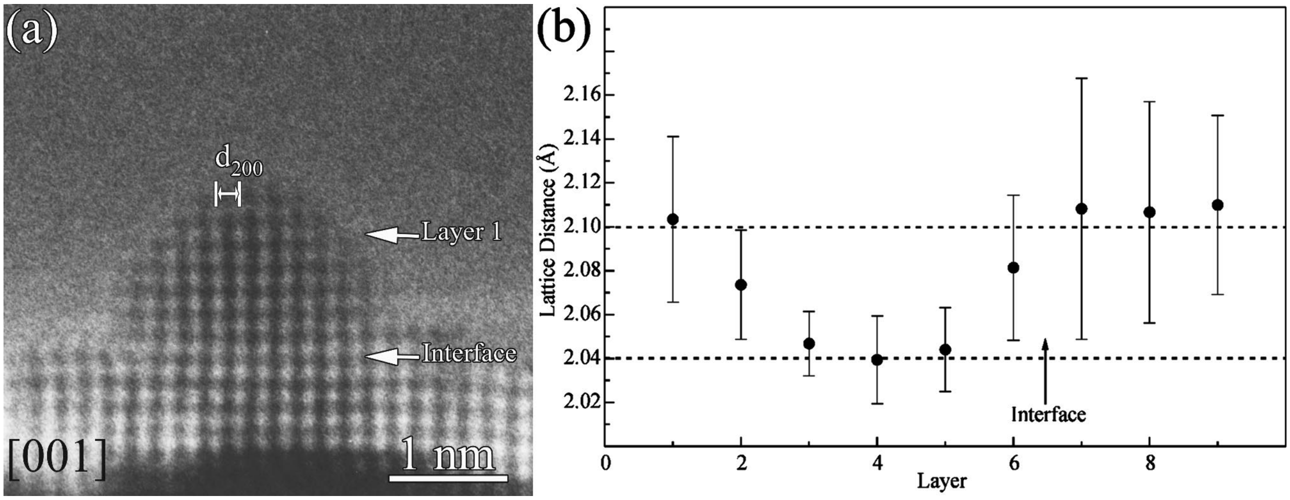

FIG. 10. (a) Cluster of six layers high on the MgO substrate. (b) Graph showing the averaged d_{200} distances of the different Au layers. The dashed lines represent the bulk MgO (2.10 Å) and Au d_{200} lattice distance (2.04 Å) and are shown for comparison.

between two or more small clusters then also clusters larger than 3 nm should be present. Also, when clusters coalesce into larger ones, planar defects (such as, e.g., stacking faults or twins) should form in the larger clusters. This is not observed for the Au clusters deposited on MgO.

B. Cluster morphology and lattice distortions on MgO

The morphology of the deposited clusters is determined by projection of the clusters perpendicular to the Au/MgO interface (cross-section) in two different orientations: ⟨011⟩ and ⟨001⟩. Also, clusters imaged in top view helped to determine the morphology. The profile of the cluster of Fig. 4(a) is limited to four ⟨112⟩ directions and two ⟨011⟩ directions; the latter two parallel to the interface and asymmetrically truncating the cluster. An ideal octahedral cluster in the [011] orientation is limited to four ⟨112⟩ directions. By truncating at the top and the interface with {001} planes, two extra ⟨011⟩ directions appear to limit the cluster profile [see Fig. 4(d)]. Figures 4(b) and 4(c) show two clusters which have both the same morphology, in cross-section view; they are smaller than the cluster shown in Fig. 4(a). From these cross-sections it is deduced that the clusters are half-octahedral shaped; the truncation at the interface has disappeared.

Figure 4(b) shows a cluster in the [011] orientation. The profile of the particle is limited to two ⟨112⟩ directions and two ⟨011⟩ directions. Viewed along the ⟨001⟩ zone axis [Fig. 4(c)], these smaller clusters are limited to two ⟨011⟩ directions and four ⟨001⟩ directions: two ⟨001⟩ directions are parallel to the interface; the other two, which arise from the truncation at the side corners, are perpendicular to the interface. In a ⟨011⟩ zone axis it is not possible to observe truncations at the side corners of octahedral clusters. Therefore, one has to observe the clusters in a ⟨001⟩ orientation. Such images show that also the side corners of the clusters are truncated. Projection of a cluster as shown in Fig. 4(a) in the [101] or [110] direction, two directions along which a top view image is obtained, should show a hexagonal profile. This is indeed often observed in HREM images (see Fig. 5).

The same morphologies for supported Au clusters are observed by several other authors,[14,17] but in these cases the clusters were fabricated by evaporation of Au atoms, which were directly deposited on the MgO cubes. With our production technique, the Au clusters are first formed in the cluster source, and then deposited by LECBD on the MgO.

All deposited clusters show the same epitaxial relation: $(001)_{\mathrm{MgO}}//(001)_{\mathrm{Au}}$ and $[100]_{\mathrm{MgO}}//[100]_{\mathrm{Au}}$. This epitaxial relation was also observed by several other authors,[14,16,17] and considered as the most stable one. This epitaxial orientation is a result of the interaction between the cluster and the MgO surface. Other epitaxies, as observed in Ref. 14, are not found in the present study.

The slowing down of metallic clusters in the LECBD regime on a metallic surface is studied in detail in Refs. 24 and 40 experimentally and by means of atomic scale modeling. No obvious relation is found between the free-flying cluster morphology—not known in the present case—and its morphology after deposition. Within the first few picoseconds of the impact, the cluster is heavily destroyed. The substrate structure and the electron-phonon coupling govern its later evolution. Modeling predicts no significant substrate damage, nor any sizable impact-induced interfacial mixing.

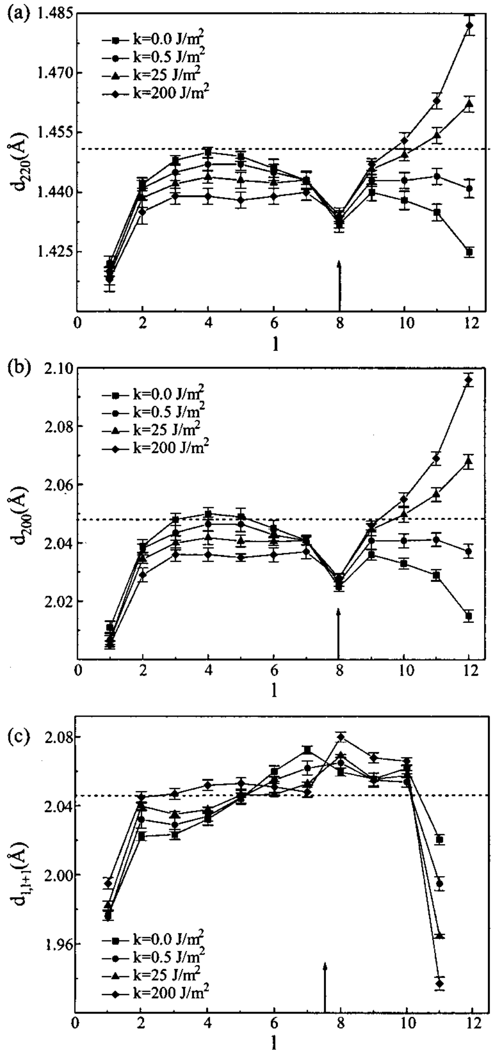

FIG. 11. Equidistances and interlayer spacing, layer by layer in the cluster, starting from the top layer of the cluster. l refers to the layer number. (a) d_{220} equidistance. (b) d_{200} equidistance. (c) $d_{l,l+1}$ interlayer spacing. The results are shown at 300 K for four k values. The dashed lines represent the bulk Au values at 300 K, as predicted by MD, and are shown for comparison. The arrows show the position of the fulcrum layer.

Here, by HREM, we studied small local dilations and contractions of the lattice of the deposited Au clusters on MgO. Because the clusters are in epitaxy with the MgO substrate, and because this substrate can be considered as a bulk material with a known lattice parameter, both the cluster and the substrate lattices can be imaged, and the distances in the Au clusters can be measured relative to the MgO distances. Figure 9(b) shows the variation of the (220) lattice distances for the Au cluster and the MgO substrate in the [011] orientation of Fig. 9(a). Layer 1 is the top layer of the cluster which consists of 11 layers. Looking at Fig. 9(a), one can say that there is another layer above layer 1. However, because it is difficult to determine the edge between the cluster and the vacuum (or to determine the first Au layer) due to edge effects, and because filtering the image introduces some extra periodicity outside the cluster, we have neglected this layer.

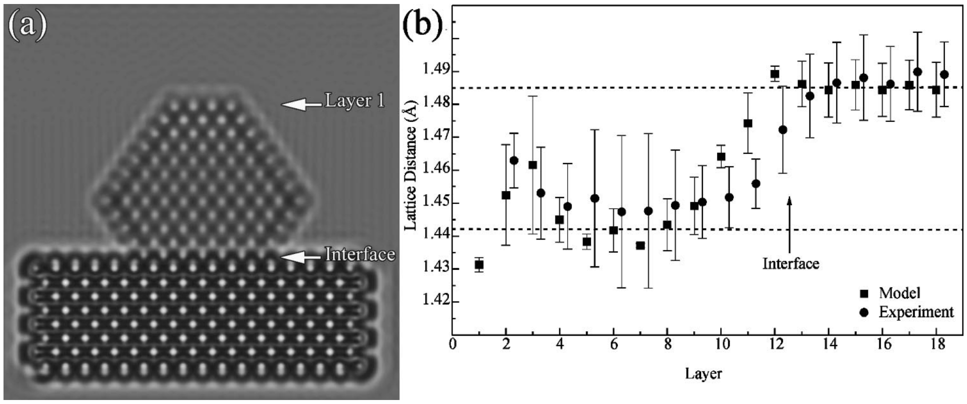

FIG. 12. (a) Simulated HREM image. The model used as input for the simulations is obtained with MD using a force constant $k = 2.0\times10^2$ J/m^2. (b) Comparison between the measured (220) distances of the experimental image of Fig. 9 and the simulated image in (a).

All layers with $n > 11$ belong to the MgO substrate. This is also seen on the graph were all layers with $n > 11$ are, within the errors, equal to 1.485 Å. The (220) distances in the Au layers close to the interface decrease from 1.472 ± 0.013 Å (in layer 11) to 1.451 ± 0.010 Å (in layer 9). For layers above ($n < 9$) the (220) lattice distance for bulk Au (1.442 Å) is reached, except for the two topmost layers. In these layers the lattice dilates by 1.4%. This is an imaging effect of the microscope, as will be discussed below.

The same behavior is also observed for clusters in a [001] orientation. Figure 10 shows a cluster of six layers high deposited on MgO, and a graph of the d_{200} distances in the cluster and the substrate. The interface is between layers 6 and 7. From the graph it can be concluded that layer 6 (2.081 ± 0.033 Å) adapts itself partially to the MgO substrate. For the other layers ($n < 6$) the d_{200} value for bulk Au (2.04 Å) is reached. Again the top two layers of the cluster are dilated by 3% due to imaging artifacts in the microscope. Such values of dilation are also observed in other studies of deposited clusters.[15]

To crosscheck the results derived from the HREM images, image simulations were made. A model of a Au cluster with bulk lattice parameters on a MgO substrate was used. From these simulations it is confirmed that the image and also the changes in lattice distances at the surface are very dependent on defocus. For several defocus values a contraction of the top layer was found; only a few values of defocus showed that the top layer could also be dilating. When measuring the d_{220} lattice distances on the simulated images, which show dilations in the top layer, these dilations are clearly visible, but no change in the (220) distances are seen near the Au/MgO interface. It is therefore concluded that the observed dilations near the Au/MgO interface are not microscope imaging effects but real changes in structure.

C. Comparison between experiments and MD

To obtain a better structure model as starting point for the image simulations, a classical molecular-dynamics simulation is used, with the previous model as starting point. The mean d_{220} and d_{200} equidistances parallel to the substrate surface are estimated layer by layer in the cluster, as well as the spacing between these layers. The spacing between layer l and layer $l+1$ is noted as $d_{l,l+1}$. The results are shown in Fig. 11 for four force-constant values. For the discussion, it is useful to section the cluster into two areas at the eighth layer, represented by an arrow in Fig. 11. This was seen in Fig. 6 to be the intersection between the {111} facets of the cluster. In the area close to the substrate, the results for $k > 0$ contrast with the free cluster, for which $k = 0$. In the latter case, d_{220}, d_{200}, and $d_{11,12}$ contract, as is typical for a free surface, while the same quantities expand for the $k > 0$ values considered. This is the direct consequence of the MgO surface, whose lattice parameter is larger than bulk Au, shown as a dashed horizontal line in Fig. 11. It is remarkable that the same three parameters in the eighth layer are independent of k, and hence, within statistical uncertainties, have the same values as in the free cluster. The deformation in this layer due to the Au/MgO interaction is thus weak in comparison with that in the other layers.

The situation is just the opposite for the series of layers further away from the substrate, that is, for layer numbers smaller than 8. d_{220} and d_{200} are close to the bulk value as the free cluster is concerned, while it is systematically smaller when $k > 0$. At the topmost layer, which contains only 16 atoms, relaxation is pronounced, and the lattice is the smallest for all the four cases. The convergence of the results in the facets intersection (layer 8), obtained with constraints of different strengths, shows that its stiffness is rather pronounced. As a consequence, it acts as the fulcrum of a lever: the increase of the equidistance on the one side, subsequent to the constraint imposed by the substrate, is balanced by their decrease on the other side. The lever effect with the facet intersection as a fulcrum is systematically found to increase with the magnitude of the force constant [Figs. 11(a) and 11(b)], which confirms the present interpretation. The relation between the lever effect and the interlayer spacing in Fig. 11(c) is less obvious, although it can be emphasized. Indeed, the effect of the substrate is to induce a pure shear in the cluster. If one considers that a shear deformation occurs at a constant volume, the increase of the equidistance parallel to the substrate surface must be balanced by a decrease in the lattice spacing normal to this surface, and vice versa. This is exactly what is seen by comparing Fig. 11(c) with Figs. 11(a) and 11(b). An examination of the numerical values of layer spacings and equidistances show this conservation to be quantitative.

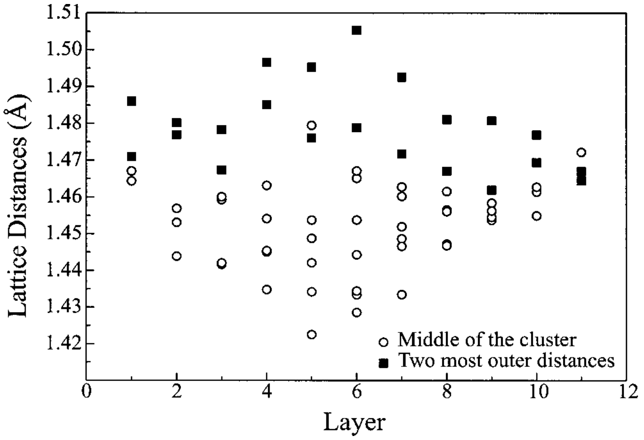

FIG. 13. Graph of the separate lattice distances measured in the different layers of the Au cluster shown in Fig. 9. The circles represent lattice distances in the middle of the cluster, and the squares represent the two outermost distances in every layer.

With the model obtained using a k value of 2.0×10^{2} J/m^{2}, HREM images were simulated following the same procedure as before. The simulated image of this model is shown in Fig. 12, together with a graph of the measured d_{220} distances in the Au cluster and the substrate. Because the outer layer of the cluster is delocalized to the outside, we do not take this layer into account when measuring the d_{220} distances. These distances are calculated in the middle part of the cluster. Figure 12(b) shows the d_{220} distances of both the experimental and simulated images. It is obvious that both the interface between Au and MgO and the lattice dilations in the cluster match very well. Only the two top layers have a d_{220} distance, which is much smaller than would be expected from the experimental image.

Another remarkable feature in both the experimental image as well as in the simulated one is the delocalization of the whole outer layer of the particle. In Fig. 13, circles represent individual lattice spacings between two neighboring bright dots in one layer for the experimental cluster image. The two squares are the two lattice spacings near the surface. It is seen that they are always larger than the other distances. The same behavior is also seen on the simulated image.

V. SUMMARY AND CONCLUSIONS

Au clusters were produced by a laser vaporization source, and were deposited with low kinetic energy onto amorphous carbon and single crystalline MgO surfaces. The individual clusters were examined by high-resolution electron microscopy. Different structures and morphologies were found for different surfaces—cubo-octahedral, decahedral, and icosahedral clusters, as well as twinned structures on amorphous carbon—while fcc truncated octahedral and truncated half-octahedral shapes were found on MgO. From a comparison between size distributions for the beam of free clusters and for the deposited clusters, it could be deduced that there is little or no cluster coagulation taking place on either surface. This was anticipated by the localizing behavior of the dangling bonds of the surface atoms in the case of amorphous carbon, and by the lattice matching condition in the case of MgO.

For cluster deposition on MgO, its well-known lattice parameter serves as an internal calibration of the HREM images, allowing a detailed investigation of dilations and contractions of the fcc lattice within the nanoparticle. The cluster structure was also simulated by classical molecular dynamics, including an effective harmonic force that describes the binding of the interfacial Au atoms to the substrate atoms. In the case of an 11-layer truncated octahedral particle, good agreement between experiment and model simulation was found. Here the result of a MD simulation using a force constant of about half the Au bulk modulus in a harmonic approximation was used as input for a HREM image simulation. Detailed investigations of equidistances parallel to the substrate and the spacings between the layers in this particle revealed a shear deformation of the clusters lattice induced by the substrate. The lattice dilation due to the epitaxial matching of Au on MgO in the layers close to the substrate goes along with lattice contractions for the upper layers. Thus the layer corresponding to the facets intersection can be seen to act as the fulcrum of a lever.

The present observations demonstrated that nanoclusters preformed in the gas phase can be deposited with LECBD on various substrates, without a measurable influence of their kinetic energy on the resulting structure or shape. More important are cluster-surface interactions as shown by the observed differences in cluster morphology for the different substrates that were used. This is corroborated by the fact that structures similar to the structures of nanoparticles grown from the gas phase are observed in the present study. With the availability of binary cluster sources, readily producing binary clusters with compositions that are not available as bulk alloys, several research opportunities open up. Further research will therefore include structural investigations of nanoalloys deposited on different substrates.

ACKNOWLEDGMENTS

B.P. and P.L. are grateful to the Fund for Scientific Research - Flanders (Belgium) for financial support. L.T.K. is grateful for grants from the Danish Research Council (SNF and STVF). This research was part of the Interuniversity Poles of Attraction Program—Belgian State, Prime Minister's Office—Federal Office for Scientific, Technical and Cultural Affairs (IUAP).

---

*Corresponding author. Email: bapauw@ruca.ua.ac.be

†Present address: Atlas Copco Airpower, Boomsesteenweg 957, B-2610, Wilrijk, Belgium.

‡Present address: Ørsted Laboratory, Universitetsparken 5, DK-2100 Copenhagen Ø, Denmark.

[1] P. Jensen, Rev. Mod. Phys. **71**, 1695 (1999).

[2] B. Yoon, V. M. Akulin, Ph. Cahuzac, F. Carlier, M. de Frutos, A. Masson, C. Mory, C. Colliex, and C. Bréchignac, Surf. Sci. **443**, 76 (1999).

[3] A. Sanchez, S. Abbet, U. Heiz, W.-D. Schneider, H. Häkkinen, R. N. Barnett, and U. Landman, J. Phys. Chem. A **103**, 9573 (1999).

[4] H. J. Fecht, Europhys. News **28**, 89 (1997).

[5] K. Højrup Hansen, T. Worren, S. Stempel, E. Lægsgaard, M.

Bäumer, H.-J. Freund, F. Besenbacher, and I. Stensgaard, Phys. Rev. Lett. **83**, 4120 (1999).

[6] C. Xu, W. S. Oh, G. Liu, D. Y. Kim, and D. W. Goodman, J. Vac. Sci. Technol. A **15**, 1261 (1997).

[7] D. Lovall, M. Buss, R. P. Andres, and R. Reifenberger, Phys. Rev. B **58**, 15 889 (1998).

[8] K. Yamamoto, Y. Kasukabe, R. Takeishi, and T. Osaka, J. Vac. Sci. Technol. A **14**, 327 (1996).

[9] S. Iijima and T. Ichihashi, Phys. Rev. Lett. **56**, 616 (1986).

[10] M. Mitome, Y. Tanishiro, and K. Takayanagi, Z. Phys. D: At., Mol. Clusters **12**, 45 (1989).

[11] L. Reine Wallenberg, Ph.D. thesis, Lund University, 1987.

[12] J.-O. Malm, Ph.D. thesis, Lund University, 1991.

[13] L. D. Marks, Rep. Prog. Phys. **57**, 603 (1994).

[14] S. Giorgio, C. Chapon, C. R. Henry, G. Nihoul, and J. M. Penisson, Philos. Mag. A **64**, 87 (1991).

[15] S. Giorgio, C. Chapon, C. R. Henry, and G. Nihoul, Philos. Mag. B **67**, 773 (1993).

[16] T. Kizuka, T. Kachi, and N. Tanaka, Z. Phys. D: At., Mol. Clusters **26**, S58 (1993).

[17] T. Kizuka and N. Tanaka, Phys. Rev. B **56**, R10 079 (1997).

[18] K. Koga, H. Takeo, T. Ikeda, and K. Ohshima, Phys. Rev. B **57**, 4053 (1998).

[19] H. Hofmeister, F. Huisken, and B. Kohn, Eur. Phys. J. D **9**, 137 (1999).

[20] H. Haberland, Z. Insepov, and M. Moseler, Phys. Rev. B **51**, 11 061 (1995).

[21] H. P. Cheng, and U. Landman, Science **260**, 1304 (1993).

[22] C. R. A. Catlow, V. L. Bulatov, and R. W. Grimes, Nucl. Instrum. Methods Phys. Res. B **122**, 301 (1997).

[23] H. Häkkinen and M. Manninen, Phys. Rev. Lett. **76**, 1599 (1996).

[24] M. Hou, Nucl. Instrum. Methods Phys. Res. B **135**, 501 (1998); H. Lei, Q. Hou, and M. Hou, Nucl. Instrum. Methods Phys. Res. B **164-165**, 537 (2000).

[25] PDF file 03-0998, Powder Diffraction File 1995, PDF 2 Database Sets 1-45, International Centre for Diffraction Data 1995 Release A6.

[26] W. Bouwen, P. Thoen, F. Vanhoutte, S. Bouckaert, F. Despa, H. Weidele, R. E. Silverans, and P. Lievens, Rev. Sci. Instrum. **71**, 54 (2000).

[27] W. Bouwen, E. Kunnen, K. Temst, M. J. Van Bael, F. Vanhoutte, H. Weidele, P. Lievens, and R. E. Silverans, Thin Solid Films **354**, 87 (1999).

[28] W. Bouwen, F. Vanhoutte, F. Despa, S. Bouckaert, S. Neukermans, L. Theil Kuhn, H. Weidele, P. Lievens, and R. E. Silverans, Chem. Phys. Lett. **314**, 227 (1999).

[29] C. Kittel, *Introduction to Solid State Physics*, 7th ed. (Wiley, New York, 1996).

[30] A. Rosenauer and D. Gerthsen, Adv. Imaging Electron Phys. **107**, 121 (1999).

[31] P. A. Stadelmann, Ultramicroscopy **21**, 131 (1987).

[32] To calculate the electron wave function, the EMS procedure pa1 is used with an accelerating voltage of 400 KeV and an absorption coefficient of 0.02 as input. The procedure im1 is used to calculate the HREM images.

[33] M. S. Daw and M. I. Baskes, Phys. Rev. Lett. **50**, 1285 (1983).

[34] F. Ducastelle, J. Phys. (Paris) **31**, 1055 (1970); M. W. Finnis and J. E. Sinclair, Philos. Mag. A **50**, 45 (1984).

[35] G. J. Ackland and V. Vitek, Phys. Rev. B **41**, 10 324 (1990).

[36] E. E. Zhurkin and M. Hou, J. Phys. Condens. Matter **12**, 6735 (2000).

[37] U. Lammers and G. Borstel, Phys. Rev. B **49**, 17 360 (1994).

[38] M. Yeadon, J. C. Yang, R. S. Averback, J. W. Bullard, D. L. Olynick, and J. M. Gibson, Appl. Phys. Lett. **71**, 1631 (1997).

[39] A. Jentys, D. H. Gray, and A. L. Rohl, Catal. Lett. **30**, 77 (1995).

[40] Q. Hou, M. Hou, L. Bardotti, B. Prével, P. Mélinon, and A. Pérez, Phys. Rev. B **62**, 2825 (2000); L. Bardotti, B. Prével, P. Mélinon, A. Pérez, Q. Hou, and M. Hou, *ibid.* **62**, 2835 (2000).